Briefings in Bioinformatics, 2026, 27, bbag416
https://doi.org/10.1093/bib/bbag416
Published: 3 August 2026
Problem Solving Protocol

OXFORD

Integrative agent-based modeling of cutaneous lupus: single-cell benchmarking and *in silico* evaluation of B-cell therapies

Abdul Wahab[1,2], Giulia Russo[2], Francesco Pappalardo[2,*]

[1]Department of Mathematics and Computer Science, University of Catania, V.le A. Doria, 6, 95125 Catania, Italy
[2]Department of Drug and Health Sciences, University of Catania, Via Valdisavoia, 5, 95123 Catania, Italy

*Corresponding author. E-mail: francesco.pappalardo@unict.it

Downloaded from academic.oup.com/bib/article/27/4/bbag416/8750276 by Universita' degli Studi di Catania user on 30 September 2026

Abstract

Agent-based models (ABMs) offer a powerful framework for representing emergent immune dynamics, yet their integration with single-cell datasets and therapeutics simulation remains limited. Here, we presented an integrative, single-cell informed systems immunology modeling framework built on universal immune system simulator (UISS) to mechanistically represent autoimmune skin inflammation specifically systemic and cutaneous lupus erythematosus. The framework incorporates (i) data-driven initialization from lesion single-cell RNA sequence cell fractions, (ii) modular immune processes coupling type I interferon signaling, ultraviolet induced keratinocyte injury, and (iii) a digital patient generation pipeline that captures inter-individual variability through stochastic parameter perturbation and quality-controlled cohort assembly. Using this platform, we constructed a cohort of 50 digital patients initially and implemented modular therapy components for B-cell Activating Factor (BAFF) neutralization (belimumab) and anti-CD20 B-cell depletion (rituximab) . *In silico*, pre–post treatment experiments revealed heterogeneous serologic responses, modest median reductions in immunoglobulin G antibodies that target the Ro/SSA protein (Ro-reactive IgG), and strong correlations between plasmablast dynamics and circulation autoantibodies, highlighting the mechanistic constraints on B-cell targeted therapies. Overall, our results demonstrated how single-cell benchmarking, rule-based immune modeling, and digital patient ensembles can be integrated into a generalizable computational workflow for studying autoimmune pathophysiology and simulating therapeutic mechanisms to explore mechanistic determinants of disease progression and therapeutic response.

Keywords **agent-based model (ABM), cutaneous lupus erythematosus (CLE), digital patients, computational immunology, B-cell targeted therapies, scRNA-seq benchmarking**

Introduction

The human immune system serves as a safeguard against invading pathogens and helps tissues recover after injury. In systemic autoimmune disease, the mechanisms that normally differentiate between harmful pathogens and the body's own tissues become disrupted. Lupus erythematosus refers to a group of autoimmune diseases, ranging from systemic lupus erythematosus (SLE), which can involve multiple organs, to cutaneous lupus erythematosus (CLE), which primarily affects the skin. CLE has been further categorized considering the clinical point of view about the emergence and progression of symptoms into acute, subacute, and chronic [1]. CLE manifestations have been classified by the clinical properties, histological, and serological subtypes, whereas butterfly rash, ultraviolet (UV) light-induced skin lesions are clinical properties, antinuclear antibodies (ANAs) specifically anti-SSA/Ro and anti-SSB/La antibodies are serological attributes, and interface dermatitis alongside the expression of interferon-regulated chemokines are histological features [2]. Combinations of various clinical, histological, and serological findings of skin lesions are subset into four groups, which are acute CLE (ACLE), subacute CLE (SCLE), intermittent CLE (ICLE), and chronic CLE (CCLE) [3]. Genetic susceptibility has a strong connection with CLE disease due to which it follows within descendants [4]. Mostly, all subset of CLE has self-reinforcing inflammatory loops which initiate between both innate and adaptive cells of immune system [5]. Primarily, engagement of these innate and adaptive cells occurs in the evolution of keratinocytic cell death, mainly due to provocation of environmental factor such as UV light which has significant impact on simulating the CLE.

Considering the complexity and heterogeneity of autoimmune diseases, such as systemic and CLE, many computational models have been introduced as a powerful framework to capture the disease patterns. Traditional experimental approaches remain fundamental, but

Received: December 17, 2025. **Revised:** April 18, 2026. **Accepted:** July 7, 2026
© The Author(s) 2026. Published by Oxford University Press.
This is an Open Access article distributed under the terms of the Creative Commons Attribution-NonCommercial License (https://creativecommons.org/licenses/by-nc/4.0/), which permits non-commercial re-use, distribution, and reproduction in any medium, provided the original work is properly cited. For commercial re-use, please contact reprints@oup.com for reprints and translation rights for reprints. All other permissions can be obtained through our RightsLink service via the Permissions link on the article page on our site—for further information please contact journals.permissions@oup.com.

at some level they are limited in their capacity to unravel the complex multi-scale and dynamic interactions between immune cells, cytokine networks, and tissue environments that drive lupus pathogenesis. To address these challenges, mathematical and computational models have been developed to simulate immune dynamics, predict disease trajectories, and explore therapeutic interventions *in silico*. Among these, agent-based models (ABMs) have proven valuable because they represent individual cells as autonomous agents governed by predefined interaction rules. In lupus research, ABMs of germinal centers have successfully reproduced the affinity maturation process and demonstrated how perturbation in T follicular helper signals, TLR 7 activation, or interferon exposure bias selection towards autoreactive B cells [6, 7]. Such models provide mechanistic explanations for the persistence of autoreactive clones and offer predictions about how therapeutic interventions targeting B-cell help or IFN pathways might alter disease outcomes. In addition to ABMs, hybrid approaches combining ordinary differential equation (ODE) models with cellular simulation have been employed to quantify systemic immune dysregulation, forecast flare occurrence, and evaluate the scheduling and dosage of immunomodulatory therapies [8, 9]. For example, model-based meta analyses of clinical trial data have been used to standardize composite endpoints in SLE, allowing quantitative assessment of drug performance across heterogeneous patient cohorts [10]. These approaches demonstrate the translational utility of computational models for both generating mechanistic hypotheses and evaluating therapeutic strategies. However, the application of ABMs specifically to CLE still remains in its early stages; the skin is a highly suitable context for computational investigation.

In this study, we extended the Universal Immune System Simulator (UISS) agent-based modeling framework to SLE, with a specific focus on CLE. UISS has been widely used to model complex immune dynamics across health and disease [11–13] and adopts a multi-layered architecture integrating physiological, disease, and therapeutic dimensions [14]. Compared with previous UISS-based autoimmune and lupus models, the present work introduces four key extensions: (i) a spatially explicit CLE lesion compartment that mechanistically represents UV-induced keratinocyte apoptosis and Ro/SSA–La/SSB autoantigen handling; (ii) an explicit B-cell targeted treatment layer for Belimumab and Rituximab, acting on BAFF-dependent survival and $CD20^{+}$ B-cell depletion at the agent level; (iii) a structured CLE-specific digital patient library, defined by biologically constrained feature vectors and designed for cohort-level simulation of flare and treatment response; and (iv) a single-cell anchored validation workflow, using single-cell RNA sequence (scRNA-seq) data from discoid lupus erythematosus (DLE) skin to constrain cell type composition, compartment structure, and UV-stress-related signatures. Building on this framework, we developed a CLE-specific disease extension that mechanistically links keratinocyte injury, type I interferon signaling, Teff/Treg imbalance, and autoantibody kinetics. This enables investigation of flare initiation and the temporal interplay between UV exposure, autoantigen release, and B-cell isotype switching. By generating digital patients, the model captures inter-individual heterogeneity in flare frequency and therapeutic response, consistent with clinical observations in CLE cohorts. Model outputs were benchmarked against scRNA-seq data from the GEO dataset GSE179633 [15], focusing on DLE skin samples to quantify cell counts and tissue fractions for direct comparison with *in silico* patients. In addition, therapeutic modules representing Belimumab and rituximab were incorporated to model BAFF inhibition and CD20+ B-cell depletion, respectively. The simulations reproduced clinically observed differences in antibody kinetics and flare recurrence, demonstrating the utility of the model for mechanistic analysis and therapeutic evaluation in CLE.

Results

We developed a dedicated disease layer within UISS for SLE, with a specific focus on modeling the pathogenesis of CLE. This layer simulates immune responses underlying CLE (Fig. 1A) by integrating key mechanisms such as autoantigen recognition, cytokine signaling, and immune cell activation, providing a comprehensive representation of CLE pathophysiology. A digital patient dataset was generated using the CLE-focused UISS ABM to capture heterogeneous disease trajectories and *in silico* responses to disease-modifying interventions.

To investigate interpatient heterogeneity, we simulated 10 digital CLE patients and tracked the Teff/Treg balance over two years (Fig. 1B). The log ratio of activated effector T cells (Teff = Th1 + Th2 + Th17) to regulatory T cells (Treg) was normalized to the median of the first 28 days. Individual trajectories were highly variable, with some patients showing sustained Teff dominance and others remaining near baseline. The cohort median exhibited a prolonged plateau followed by gradual decline, while the IQR widened after 400 days, indicating divergent disease courses. These patterns mirror clinical CLE and SLE heterogeneity, where impaired Treg function contributes to persistent immune activation and variable flare frequency, remission duration, and treatment response [16–18].

Cutaneous lupus erythematosus-agent-based model simulated disease layer dynamics

Autoantigen-driven antibody dynamics co-vary with modeled flare intervals

We analyzed immunoglobulin G (IgG) production as a marker of B-cell activation and autoantibody burden. Mean ± SD IgG levels from 10 digital patients over a 2-year simulation captured substantial interpatient variability (Fig. 1C). IgG remained low during the early phase (0–100 days), increased steadily between days 100–400, and reached a plateau ∼100 000 units, with variability widening over time, indicating heterogeneous autoreactive B-cell expansion. This pattern mirrors clinical CLE and SLE observations, where IgG autoantibodies progressively accumulate and persist with marked patient-to-patient variability [19, 20].

Using autoantigen time series from a representative digital patient (RS 711), we derived antibody proxies reproducing expected immunoglobulin dynamics (Fig. 1D). Autoantigen levels rose rapidly and then declined; the IgM proxy increased transiently and resolved within weeks, whereas the IgG proxy emerged after a delay, plateaued, and declined slowly. Flares, defined by a Teff-based criterion, clustered during periods of sustained IgG and along the autoantigen decay phase, consistent with CLE/SLE immunopathology driven by immune-complex formation and complement activation despite declining antigen levels [21]. Minor late IgG increases likely reflect intermittent antigen exposure and BAFF-supported plasma-cell survival, aligning with persistent lupus autoantibody seropositivity [22].

Ultraviolet-induced keratinocyte injury sustains antigen availability and immune activation

Simulation of the skin compartment showed that the total keratinocyte pool remained stable over 2 years, indicating preserved epidermal

Downloaded from academic.oup.com/bib/article/27/4/bbag416/8750276 by Universita' degli Studi di Catania user on 30 September 2026

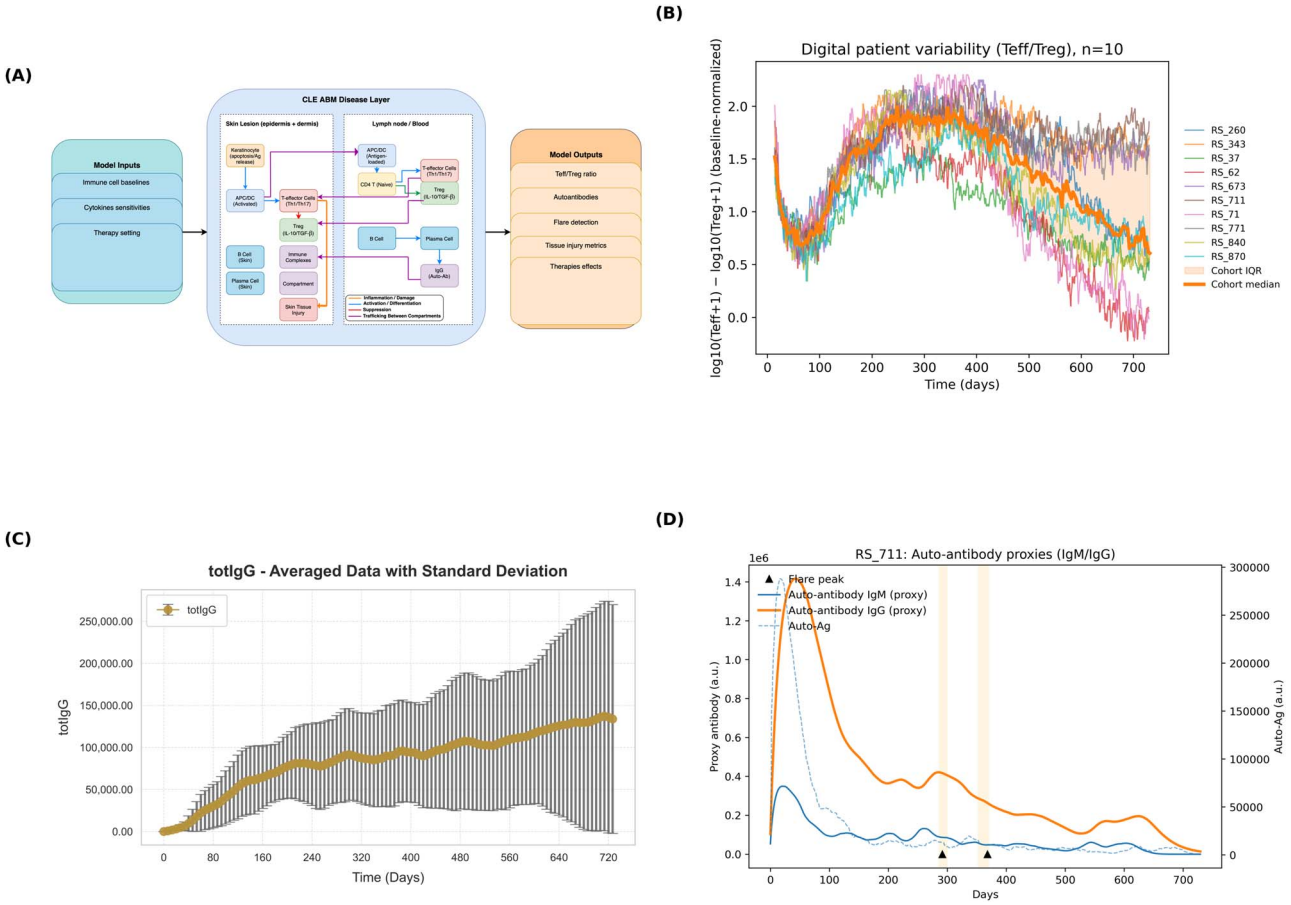


Figure 1 Workflow of CLE ABM. (A) Architecture of the CLE ABM. Left: model inputs used to initialize each digital patient (immune cell baselines, cytokine sensitivities, and therapy regimen). Center: the disease layer having two compartment representation of a cutaneous lesion (epidermis + dermis) and the lymph node/blood compartment. Keratinocyte UV injury releases autoantigens that are captured by APCs, driving CD4+ T-cell priming (Th1/Th17 versus Treg), B-cell activation and plasma cell differentiation; plasma cells secrete antigen-specific IgG and immune complexes feedback to amplify tissue injury. Right: model outputs (Teff/Treg balance, autoantibody trajectories, flare metrics, tissue-injury indices, and simulated therapy effects). Color coding denotes major process classes: inflammation/damage, activation/differentiation, suppression, and inter-compartment trafficking. (B) Digital patient variability in Teff/Treg balance. Ten digital CLE patients were simulated using the ABM framework. Activated Teff (Th1+Th2+Th17) and Treg counts were combined into a log ratio metric, baseline normalized to the first 28 days. Thin colored lines represent individual patients (RS_xxx), the thick orange line indicates the cohort median, and the shaded region shows the interquartile range (IQR). While the cohort median revealed a broad Teff/Treg imbalance between days 150–400, substantial inter patient variability was observed, reflecting heterogeneous disease trajectories like those seen in CLE patients. (C) Dynamics of IgG production across digital CLE patients. The curve represents the average IgG levels across 10 digital patients over 720 days (2 years), with shaded areas indicating the standard deviation. IgG titers progressively increased over time, reflecting sustained B-cell activation and pathogenic autoantibody production. Variability across simulations mirrors the heterogeneity of autoantibody responses reported in clinical CLE cohorts. (D) Antigen drive, antibody kinetics, and flare timing in a digital CLE patient (RS_711). Autoantigen signal (dashed line) peaks early after modeled UV-induced keratinocyte damage and then decreases with minor fluctuations. The IgM proxy (blue) rises rapidly and then decays, while the IgG proxy (orange) appears with a delay, reaches a broad plateau, and declines slowly. Vertical shading marks flare intervals detected by the Teff-threshold algorithm; black triangles indicate flare peaks. The kinetic ordering (IgM, IgG) and the concurrence of flares with sustained IgG are consistent with immune complex-mediated injury in CLE. Proxies are in arbitrary units and reflect model-derived dynamics rather than absolute concentrations.

homeostasis despite repeated UV injury (Fig. 2A). In contrast, keratinocyte MHC-I and MHC-II expression displayed recurrent fluctuations, accompanied by an early burst of acute cell death followed by persistent low-grade chronic loss. These dynamics indicate that epidermal integrity is maintained while intermittent antigen presentation and autoantigen leakage persist, sustaining dendritic-cell activation, and type-I interferon signaling. This behavior mirrors CLE pathogenesis, where UV-triggered keratinocyte apoptosis exposes Ro/SSA and La/SSB antigens and promotes interferon-driven inflammatory cascades that predispose to immune-mediated flares [22].

Sustained antigen presentation drives chronic immune activation

Across simulations, antigen persistence was associated with stable yet activated antigen-presenting cell and T-helper compartments (Fig. 2B–D). Dendritic cells maintained sustained MHC-II and co-stimulatory activity, supporting continuous CD4+ T-cell priming, while T-helper populations exhibited a persistent Th1/Th17 bias with insufficient regulatory control. Together, these dynamics establish a self-reinforcing inflammatory environment consistent with CLE lesions, in which antigen persistence, interferon signaling, and effector-dominant T-cell responses drive chronic tissue inflammation [23–28]. Cell type

Downloaded from academic.oup.com/bib/article/27/4/bbag416/8750276 by Universita' degli Studi di Catania user on 30 September 2026

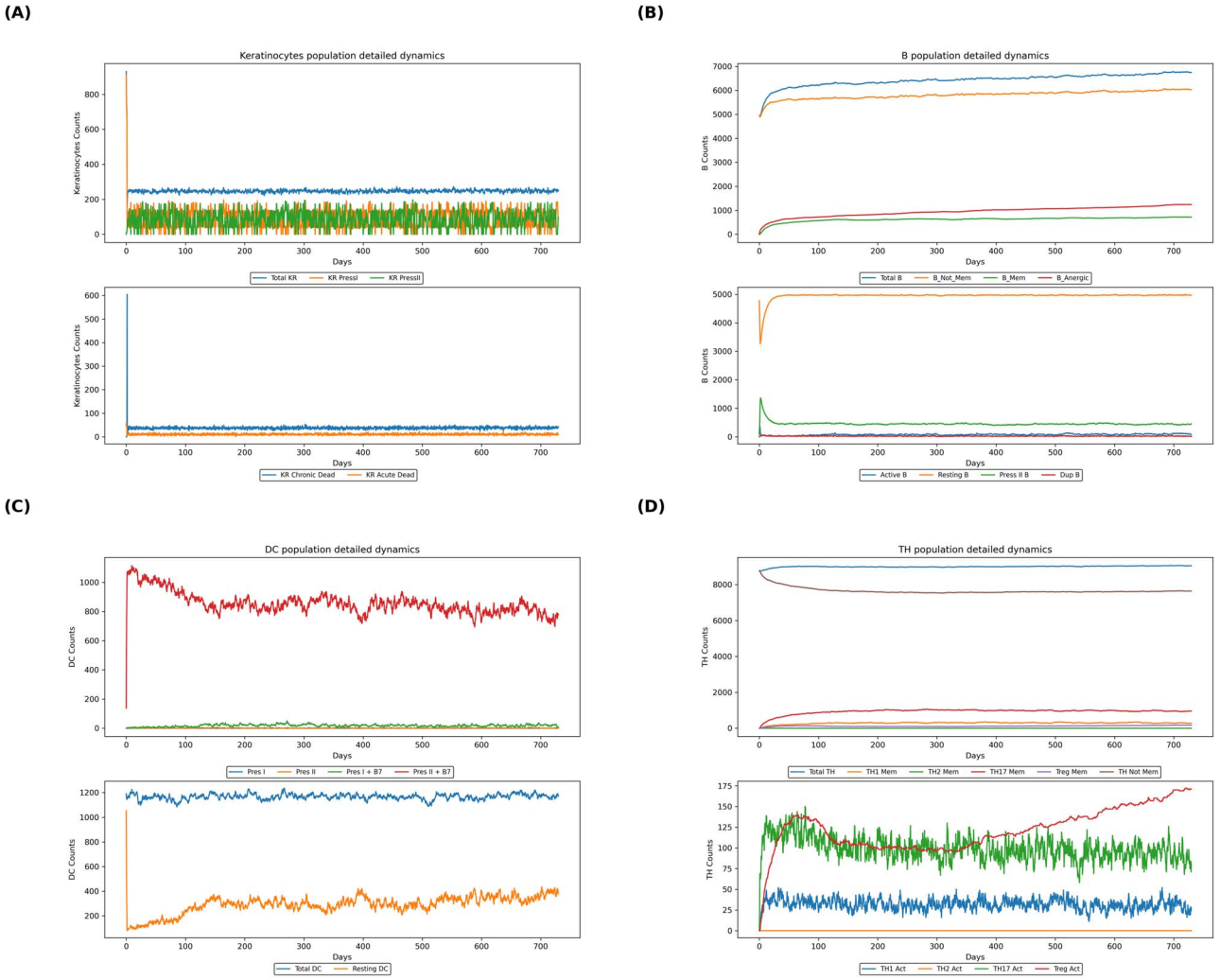


Figure 2 Illustration of the mechanistic time evolution of key immune compartments within the CLE disease layer. (A) Keratinocyte population and death modes in the CLE skin compartment due to UV radiation. Top: Total keratinocyte counts remain broadly stable, whereas the numbers presenting antigen via MHC-I and MHC-II fluctuate, indicating intermittent up-regulation of antigen presentation. Bottom: A prominent early acute-death spike is followed by a low baseline, while chronic death persists at low levels with gradual accumulation. The combination of epidermal homeostasis with episodic presentation and continual low-level loss suggests a sustained autoantigen supply that can maintain interferon programmed inflammation and flare susceptibility. Curves are model outputs (arbitrary units) from a representative single digital patient. (B) B-cell population dynamics in a digital CLE patient. Top: Total B-cell count on the x-axis rises rapidly and plateaus while simulating over 700 days. Nonmemory B-cells dominate and remain stable; memory B cells increase gradually; anergic B cells accumulate over time. Bottom: The pool is largely resting; small, fluctuating active B-cell fractions occur irregularly. MHC-II positive antigen presenting B cells persist at moderate levels, whereas actively duplicating B cells are rare. This composition supports ongoing antigen presentation with slow memory accrual, providing a systematic link to sustained IgG responses and increased susceptibility to flare. (C) Dendritic cell (DC) population dynamics in a digital CLE patient. Top: Antigen-presenting subsets showed differential trajectories, with MHC-I DCs (blue) and MHC-II DCs (orange) remaining stable, while co-stimulatory MHC-II+B7 DCs (red) persisted at elevated levels after an initial sharp rise. Bottom: The total DC pool (blue) stabilized ∼1200 cells, while resting DCs (orange) remained consistently present, reflecting turnover, and replenishment. These patterns indicate continuous antigen presentation and co-stimulatory signaling, consistent with lupus immunopathology. Absolute counts are internal model units and interpretation focuses on relative state occupancy and persistence. (D) T-helper (Th) cell population dynamics in a digital CLE patient. Top: The total Th population (blue) stabilized ∼9000 cells, dominated by nonmemory subsets (brown). Memory Th1 (orange), Th2 (yellow), Th17 (green), and Treg (purple) populations remained at lower levels, with modest increases in Th1 and Th17 memory cells over time. Bottom: Activated subsets revealed persistent Th1 (blue) and Th17 (green) dominance, oscillating across the simulation, while Tregs (red) gradually increased but remained lower, indicating limited suppressive compensation. Th2 activity was negligible. The imbalance between effector and regulatory subsets reflects the pathogenic Th1/Th17 bias observed in CLE.

resolved dynamics for B cells, dendritic-cell subsets, and Th/Treg populations are reported in (Supplementary Results. B cell, dendritic cell, and Th/Treg Subsets Dynamics). Validating with scRNA-seq GSE179633 provides cross-sectional lesion snapshots rather than longitudinal trajectories, therefore, we use (Fig. 2B and C) to illustrate mechanistic time evolution, while validating model realism by comparing steady-state cellular fractions and antigen-presentation programs against scRNA-seq profiles (Fig. 3).

Downloaded from academic.oup.com/bib/article/27/4/bbag416/8750276 by Universita' degli Studi di Catania user on 30 September 2026

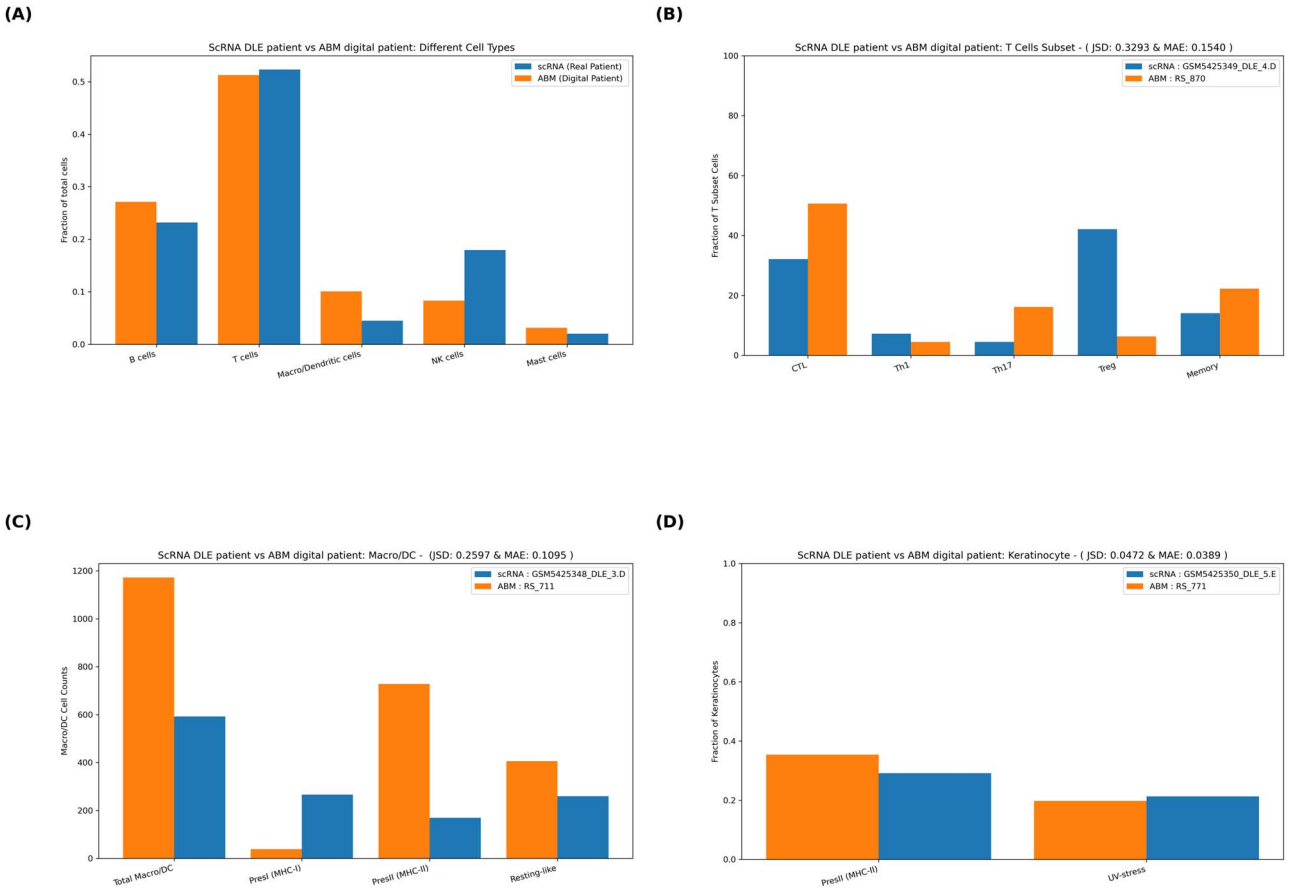


Figure 3 Benchmarking ABM model against scRNA-seq. (A) Major cell type composition in DLE: ABM digital patients versus scRNA-seq cohort. Bar chart shows cohort median fractions of B cells, T cells, Macrophage/Dendritic cells, NK cells, and mast cells from 10 ABM digital patients (blue) and 10 DLE scRNA-seq samples from GSE179633 (orange). Both modalities highlight T cells as the predominant compartment, with modest differences in B cells and NK cells, and a cohort-level shift in the Macro/DC fraction. For patient-level matching, we computed the JSD and MAE between ABM and scRNA class distributions. (B) T-cell subtype fractions: ABM digital patient versus scRNA-seq sample from GSE179633 as a DLE lesion. A bar plot compares the percentages of CTL, Th1, Th17, Treg, and Memory T cells between one ABM digital patient (orange; RS_870) and a matched scRNA-seq sample from GSE179633 (blue; GSM5425349_DLE_4.D). Values are fractions within the T-cell compartment. Agreement metrics are shown above (MAE = 0.1540, JSD = 0.3293). The ABM over-represents CTL and Th17 and under-represents Treg relative to the biopsy. In DLE skin, cytotoxic/TRM programs are common, but lesions are generally Th1 leaning with variable Th17 and context-dependent Treg abundance/function, motivating targeted parameter refinements. (C) Macro/DC presentation states in a DLE lesion: ABM versus scRNA-seq. Bar plot compares Total Macro/DC, PresI (MHC-I), PresII (MHC-II), and Resting-like counts for one ABM digital patient (orange; RS_711) and a matched scRNA-seq sample from GSE179633 (blue; GSM5425348_DLE_3.D). Agreement metrics are shown above (MAE = 0.1095, JSD = 0.2597). The ABM produces higher overall Macro/DC counts and favors MHC-II presenting and resting-like states, whereas the biopsy shows relatively more MHC-I cross-presenters. Differences are consistent with reported myeloid heterogeneity and interferon-linked dendritic cell activation in CLE skin. (D) Keratinocyte programs in a DLE lesion: ABM versus scRNA-seq. Bar plot shows the fraction of keratinocytes classified as PresII (MHC-II) and UV-stress for one ABM digital patient (orange; RS_771) and a matched scRNA-seq sample from GSE179633 (blue; GSM5425350_DLE_5.E). Agreement is high (MAE = 0.0389; JSD = 0.0472). The ABM modestly overestimates MHC-II–positive keratinocytes, whereas the biopsy has a slightly larger UV-stress fraction, both patterns consistent with reports of HLA-DR expression in keratinocytes from lupus lesions and UV-triggered IFN programs in CLE skin.

Benchmarking agent-based model model against single-cell RNA-seq skin data in discoid lupus erythematosus cohort (GSE179633)

We compared major cell populations between 10 agent-based (digital patients) and 10 DLE samples from the GSE179633 single-cell dataset [15]. For benchmarking against scRNA-seq, ABM-derived cellular fractions were averaged over days to reduce stochastic fluctuations, during which immune compartments fluctuate around stable quasi–steady state means, as illustrated in (Fig. 2). Cohort medians showed close agreement for T-cell abundance (ABM 0.51 versus scRNA 0.52 of total cells), consistent with prior reports that T cells are dominant in cutaneous lupus lesions (Fig. 3A). Because scRNA-seq data are affected by batch variability and sampling depth, concordance was interpreted at the level of dominant compartment hierarchy (e.g. T-cell predominance) rather than exact proportional matching of rare subsets. This approach reduces sensitivity to technical noise while preserving biologically meaningful structural comparisons. B cells were slightly higher in the ABM than in scRNA, which remains compatible with the known B-cell enrichment in DLE skin. The substantial cohort level difference appeared in the myeloid compartment macrophages and dendritic cells (Macro/DC), with the ABM predicting higher fractions than the scRNA median. These results align with single-cell and histologic studies, as reported in published research, which indicates that myeloid involvement in CLE is highly variable, particularly for pDC, cDC, and macrophage subsets [29]. Our findings

Downloaded from academic.oup.com/bib/article/27/4/bbag416/8750276 by Universita' degli Studi di Catania user on 30 September 2026

suggest refining the parameters for myeloid recruitment, survival, and IFN-driven loops to better reflect observed heterogeneity. Natural killer (NK) and mast cells represented minor compartments in both modalities, with scRNA showing relatively more NK cells. This finding aligns with emerging single-cell descriptions of NK subsets in CLE but indicates that NK activation may be underrepresented in the current model [30].

We quantified agreement between each digital patient and the single cell biopsy profiles using two complementary distributional metrics, the Jensen–Shannon distance (JSD) and the mean absolute error (MAE) of per-cell class fractions (Supplementary Figs S1 and S2). The JSD is bounded between 0 (identical distributions) and 1 (maximally divergent distributions). In practice, JSD values below ~ 0.2 are typically interpreted as indicating strong similarity between probability distributions, whereas values between ~ 0.2 and 0.4 reflect moderate divergence and values above ~ 0.5 indicate substantial mismatch. In our cohort level comparisons, several digital patients achieved JSD values in the range ≈ 0.15–0.25 relative to specific DLE biopsies, indicating close to moderate agreement in overall cellular composition.

The MAE provides complementary information in absolute fraction units. For example, an MAE of 0.05 corresponds to an average 5% absolute difference per major cell class. Best-matching digital patients exhibited MAE $\approx$ 0.03–0.08 (3–8% average deviation per class), whereas less similar pairings approached MAE $\approx$ 0.20–0.25 (20%–25% deviation), reflecting biologically meaningful shifts in compartment composition. Given the known inter-lesional heterogeneity in DLE and technical variability inherent to scRNA-seq sampling, JSD values in the 0.15–0.25 range and MAE values below 0.1 indicate that the model captures the dominant cellular hierarchy and relative compartment structure while preserving realistic variability.

Subcluster-level validation against matched discoid lupus erythematosus scRNA-seq biopsies (GSE179633)

We performed subcluster-resolved comparisons between one ABM digital patient and a matched DLE biopsy from GSE179633 [15], focusing on T-cell, myeloid (Macro/DC), and keratinocyte programs (Fig. 3B–D). For T-cell subtypes (Fig. 3B), the ABM reproduced the overall T-cell structure but showed shifts consistent with known CLE variability, including higher CTL and Th17 fractions and lower Treg relative to the biopsy, while Th1 remained modest; these deviations are biologically interpretable given lesion heterogeneity and reported variability in Th1/Th17/Treg balance in DLE/CLE [31, 32]. For Macro/DC presentation states (Fig. 3C), the ABM broadly matched the myeloid burden but favored MHC-II–associated and resting-like states over MHC-I cross-presenting states, a relevant control point for downstream CD4/CD8 polarization and local IFN amplification in CLE [33, 34]. In contrast, keratinocyte programs (MHC-II and UV-stress) showed close agreement between ABM and biopsy (Fig. 3D), consistent with evidence for HLA-DR+ keratinocytes and UV-driven stress/IFN checkpoints in lupus skin [35, 36].

Detailed subcluster fractions, divergence metrics, and extended analyses are provided in the (Supplementary Results. Subcluster-level benchmarking against matched DLE scRNA-seq biopsies).

Simulation of personalized therapy belimumab on digital patients

We simulated Ro/SSA and La/SSB-specific IgG dynamics in 50 independent digital patients treated with belimumab (subcutaneous: 400 **mg** × 4 loading doses, then 200 **mg** weekly, starting at day 28) and computed percent change from baseline over two years. Ro/SSA specific IgG (Ro_IgG) and corresponding plasma B cells (PLB_Ro_IgG) were tracked (Fig. 4A). Median Ro_IgG increased over time in both pre and post therapy arms, with the post-therapy median modestly lower during months 2–12 but largely overlapping the pretherapy IQR, indicating limited median reduction and persistent inter-individual variability.

To quantify individual outcomes, we computed paired percent changes (post versus pre) at days $\{7, 28, 84, 168, 365\}$ revealed wide heterogeneity (Fig. 4B): some simulations showed substantial declines (up to $\sim$ 40% at day 365), whereas many exhibited minimal change or increases. At 1 year, the median change was modestly negative **median** $\approx -3.6\%$ (bootstrap 95% CI: $[-11.3\%, +0.6\%]$; $N = 50$). Plasma B (PLB) (`PLB_Ro_IgG` closely correlated with circulating `Ro_IgG` median Pearson $r > 0.98$), and paired pre/post comparisons at day 365 showed a strong linear relationship (best fit slope < 1, Pearson $r \approx 0.93$), consistent with a global downward shift while preserving patient ranking (Fig. 4C).

The per-simulation heatmap (Fig. 4D) reveals structured heterogeneity rather than random dispersion. Early time points (days 7–28) show minimal deviation from baseline across most digital patients, consistent with delayed pharmacodynamic effects. By days 84–168, a subset of simulations exhibits moderate to marked reductions, while others remain near baseline or increase, producing a vertically stratified pattern. At day 365, responses remain heterogeneous, with no uniform cohort-level suppression. This pattern indicates that belimumab efficacy in the model depends on underlying immune composition (e.g. BAFF-sensitive plasmablast dominance versus long-lived plasma cell (LLPC) persistence), rather than producing uniform serologic decline. Comparison with clinical data highlights that, unlike anti-dsDNA antibodies which show larger median reductions, anti-Ro/SSA and anti-La/SSB antibodies are typically stable over time and weakly correlated with disease activity, remaining largely unchanged during BAFF blockade, consistent with published SLE/CLE studies [37–40]. These comparisons are qualitative and intended to assess biological plausibility rather than to reproduce specific clinical trial effect sizes. Formal quantitative calibration against longitudinal belimumab trial datasets was not performed in the present study.

Simulation of personalized therapy rituximab on digital patients

We simulated Rituximab therapy as a discrete, scheduled B-cell depleting intervention, with each dose represented as a bolus 1000 mg = 1 000 000 μg in model units) delivered at days 28 and 42 (induction) and at $\sim$6 and 12 months (days 210 and 395) for maintenance. Consistent with anti-CD20 specificity, plasmablasts and LLPCs were not directly targeted.

Cohort median trajectories of Ro-specific IgG and plasma B cells (PLB_Ro_IgG) are shown in (Fig. 5A). Median Ro_IgG increased over two years in both pre and post therapy arms, with the post-therapy curve modestly lower during months 2–12 but largely overlapping the pretherapy IQR. Paired percent changes (post versus pre) at days 7, 28, 84, 168, and 365 exhibited substantial inter-individual variability (Fig. 5B). At 1 year, the median change was -4.0% (IQR $\approx -18.7\%$–$+12.4\%$) Bootstrap 95% CIs $[-8.7\%, +6.3\%]$, and Wilcoxon paired tests were nonsignificant at all time points ($P \gg .05$).

Pre versus post therapy Ro_IgG at day 365 showed a strong linear relationship (slope $\sim$ 1.14, Pearson $r \approx 0.93$), indicating a

Downloaded from academic.oup.com/bib/article/27/4/bbag416/8750276 by Universita' degli Studi di Catania user on 30 September 2026

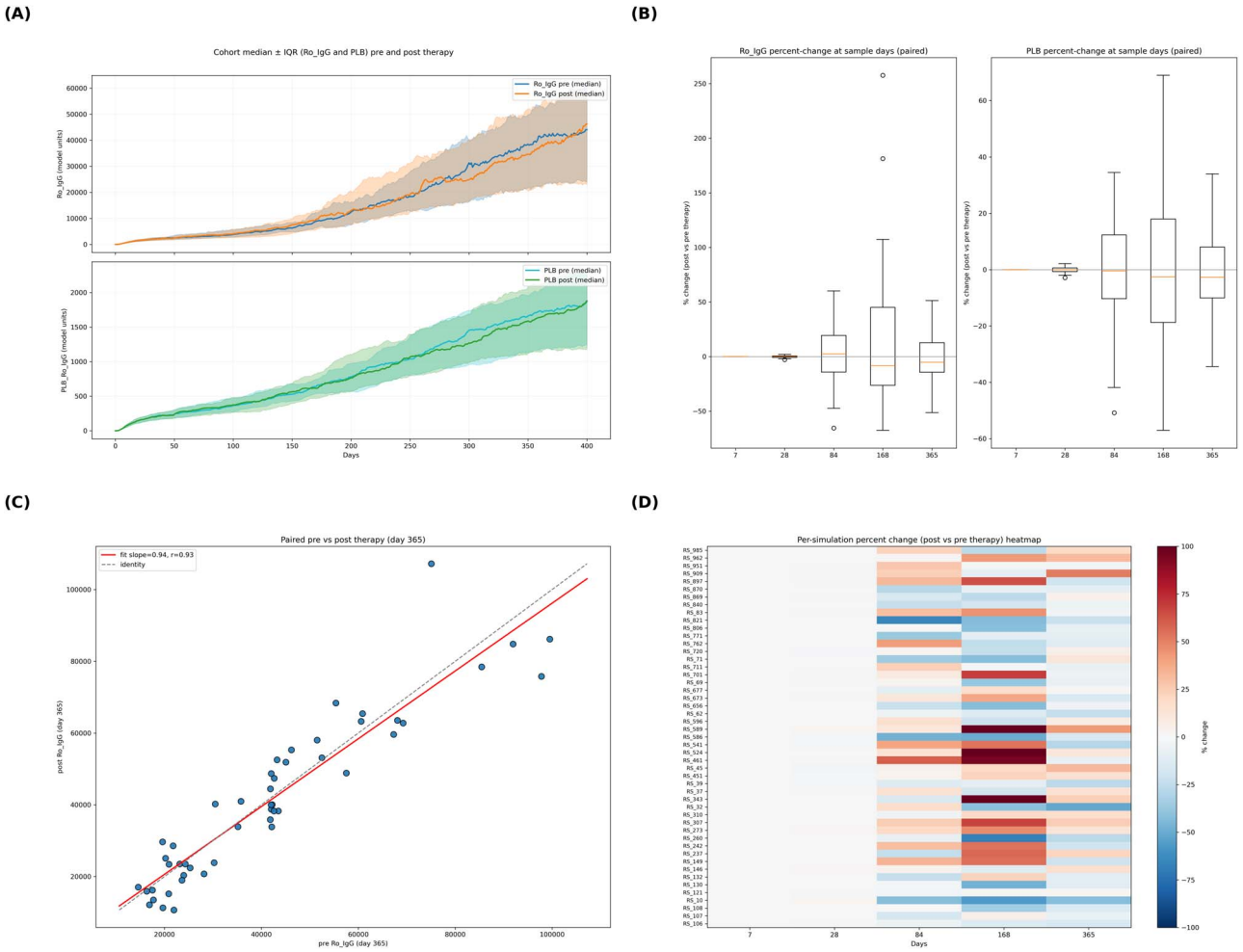


Figure 4 Simulation of personalized therapy belimumab on digital patients. (A) Top: cohort median Ro_IgG (solid lines) with IQRs (shaded areas) for the pretherapy (blue) and post-therapy (orange) arms across $n = 50$ digital patients. The vertical dashed line marks the first belimumab dosing (day 28). Early dynamics are similar across arms; from ∼2–12 months, the post-therapy median is modestly lower than the pretherapy, but the IQRs overlap substantially, indicating pronounced individual variability. Bottom: cohort median ± IQR for Ro-specific plasma B cells (PLB_Ro_IgG) showing population-level PLB suppression after BAFF neutralization together with wide between-run spread. (B) Boxplots show the distribution of per-run percent changes (post relative to pre) at days 7, 28, 84, 168, and 365 for Ro_IgG (left) and PLB_Ro_IgG (right). Early timepoints (7 and 28 days) exhibit mostly small changes across the cohort; variability increases at 84 and 168 days, with several outliers showing pronounced declines or rises. By day 365, the cohort median percent change is modestly negative, while the IQR spans both decreases and increases, illustrating that large serologic reductions are observed in only a subset of simulations. (C) Each point represents a single digital patient's pretherapy and post-therapy Ro_IgG values measured at day 365. The red line is the linear least-squares fit (slope ≈ 0.94), and the dashed gray line is the identity. The strong Pearson correlation ($r \approx 0.93$) together with a slope slightly below unity indicates that belimumab produces a modest, approximately uniform downshift in Ro_IgG while largely preserving the relative ordering of patients (high pretherapy responders tend to remain relatively high post-therapy). (D) Heatmap of per-run percent change in Ro-specific IgG (post versus pretherapy) at standard sampling times (7, 28, 84, 168, and 365 days after therapy start). Each row corresponds to one digital patient (labeled RS_XXX) and colors show percent change (red = increase, blue = decrease; scale -100% to $+100\%$). The map highlights large inter-individual variability: many runs show modest changes, while some runs exhibit pronounced reductions (dark blue) or increases (dark red), particularly at intermediate time points (84–168 days). Vertical ordering is by run identifier; columns are the sampling days. Together, the panels show a modest median serologic reduction with large inter-individual variation.

global shift with preserved patient ranking (Fig. 5C). The Rituximab heatmap (Fig. 5D) demonstrates a similar but mechanistically distinct pattern. While transient intermediate term declines are observed in a subset of digital patients, long-term effects remain variable, reflecting incomplete suppression of IgG production due to persistence of $CD20^-$ negative plasma cells. The wide dispersion at later time points underscores that $CD20^+$ depletion alone does not guarantee durable serologic reduction in the presence of long-lived plasma compartments. Sensitivity analysis further showed that only a minority of digital patients achieved large serologic reductions. Finally, sensitivity analysis of responder fraction versus responder threshold (Supplementary Fig. S4) shows that the fraction classified as responders falls rapidly as the threshold increases: (e.g. ∼45% of runs show at least a 5%–10% decrease at day 365.

These results reproduce the expected mechanism of rituximab, which depletes circulating CD20+ B cells while sparing LLPCs that sustain IgG production. The heterogeneous responses align with clinical observations linking incomplete B-cell depletion and LLPC persistence to variable serologic outcomes and relapse risk [41], supporting the biological plausibility of the model. Similarly, the rituximab

Downloaded from academic.oup.com/bib/article/27/4/bbag416/8750276 by Universita' degli Studi di Catania user on 30 September 2026

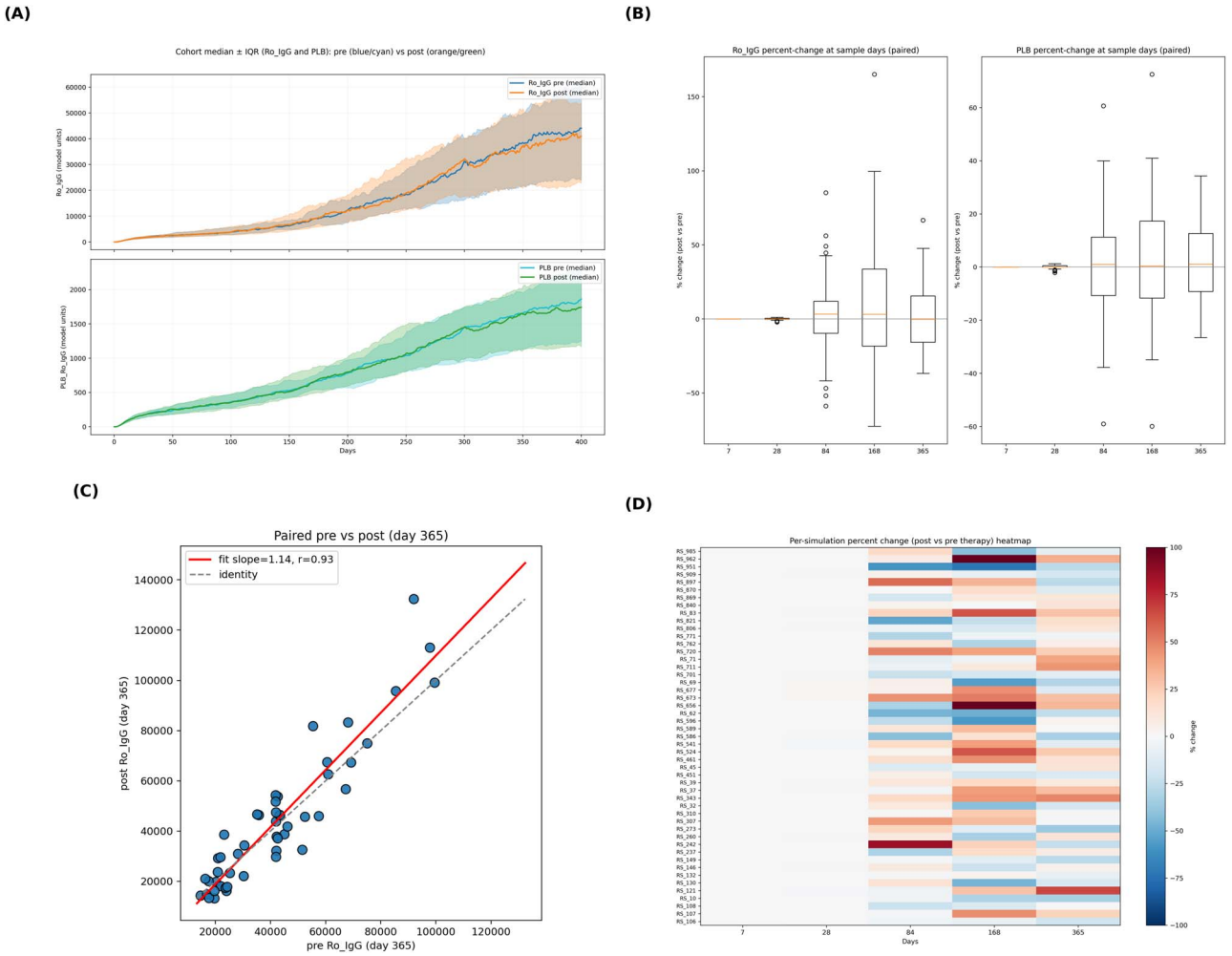


Figure 5 Simulation of personalized therapy rituximab on digital patients. (A) Top panel: cohort median and IQR of Ro_IgG before (blue) and after (orange) therapy. Vertical dashed line marks therapy start (day 28). Bottom panel: cohort median and IQR for Ro-specific plasmablasts (PLB_Ro_IgG). Shaded IQR bands indicate inter-run variability. The post-therapy median is modestly lower than pre for much of months 2–12, but the IQRs overlap extensively, showing large inter-individual heterogeneity. (B) Boxplots show the distribution of per-run percent changes (post relative to pre) Left: distribution of per-run percent change (post versus pre) for Ro_IgG at sample days 7, 28, 84, 168, and 365 after therapy start. Right: equivalent panel for PLB_Ro_IgG. Boxes show the IQR and medians (orange). Many runs cluster near zero but the spread grows at intermediate timepoints (84–168 days), indicating heterogeneous per-run responses. (C) Scatter of pre versus post Ro_IgG (same day, day 365) for all runs passing QC. Red line: linear fit (slope reported in panel); dashed gray: identity. Strong linear association (Pearson $r \approx 0.93$) indicates therapy produces a global shift while largely preserving ranking across patients. (D) Heatmap of per-run percent change in Ro-specific IgG (post versus pre therapy). Rows indicating individual digital patients (labels RS_XXX). Columns representing sample days (7, 28, 84, 168, and 365). Colors are showing percent change (red = increase, blue = reduction; range shown -100% to $+100\%$). The map highlights that a minority of runs show large reductions (dark blue) at intermediate times while many runs show little change or increases, producing only a modest median effect at day 365.

simulations were designed to evaluate mechanistic depletion effects and inter-individual variability rather than to replicate specific clinical response rates or serologic endpoints reported in randomized trials.

Discussion

Previous computational models of SLE have primarily focused on systemic immune compartments using ODE-based approaches, and prior UISS implementations did not explicitly represent a skin resident disease layer, the present work introduces a bidirectionally coupled architecture linking UV-induced keratinocyte injury in the epidermis and dermis with systemic lymphoid activation. This enables mechanistic simulation of local systemic feedback loops, interferon amplification, antigen presentation polarity, and B-cell driven autoantibody dynamics under therapeutic perturbation. In this work, to validate the proposed model, we tested whether the CLE ABM reproduces the cellular landscape observed in scRNA-seq from DLE lesions. Across major cell classes (T, B, myeloid, keratinocyte, NK, and mast), the ABM captured the observed hierarchy, with T cells dominating, followed by B cells and myeloid populations. Cohort-level T-cell fractions closely matched biopsy data, indicating disease-specific rather than generic agreement. Where discrepancies occurred, they were moderate by distributional metrics (JSD/MAE) and biologically interpretable. The model performed particularly well for epithelial programs: keratinocyte MHC-II (PresII) and UV-stress states closely aligned with biopsy data, showing minimal error and capturing key antigen-presentation and interferon-related checkpoints. At the subtype level, the ABM tended to overestimate CTL and Th17 cells and

Downloaded from academic.oup.com/bib/article/27/4/bbag416/8750276 by Universita' degli Studi di Catania user on 30 September 2026

underestimate Tregs; within the myeloid pool, it favored MHC-II presenting and resting states over MHC-I cross-presenting subsets. These differences identify specific calibration targets, including modulation of Th17 maintenance, cytotoxic licensing, Treg expansion, and DC subset kinetics. Residual discrepancies likely reflect lesion heterogeneity and scRNA-seq technical limits. We therefore treat these gaps as calibration objectives and tune the model against cohort summaries rather than individual biopsies to capture patient-to-patient variability. In addition, the reference scRNA-seq dataset is subject to technical variability, including batch effects, differential capture efficiency, and dissociation bias, which may influence observed cell type proportions. Our benchmarking therefore prioritizes major compartment structure and distributional similarity rather than exact matching of rare subsets.

We implemented a CLE-focused therapy layer within the ABM to simulate Ro/SSA and La/SSB autoantibody dynamics under standard belimumab treatment. Belimumab neutralizes soluble BAFF, reducing survival and differentiation of naïve and activated B cells and lowering circulating plasmablasts, producing progressive reductions in some serologic markers in clinical studies, consistent with model outputs [37, 42]. However, LLPCs residing in survival niches are largely BAFF-independent and can sustain antibody production for extended periods, limiting serologic change after BAFF blockade alone [43]. For Ro/SSA and La/SSB, UV-driven keratinocyte antigen release sustains local immune activation; thus, belimumab is predicted to reduce autoantibody levels mainly in patients whose responses are dominated by BAFF-sensitive plasmablasts, with limited effects in LLPC-dominated cases [44]. To demonstrate therapeutic modularity and contrast BAFF neutralization, we also implemented an anti-CD20 (rituximab) module that depletes CD20+ B cells while sparing plasma cells. Paired pre–post simulations using identical cohort generation and dosing schedules showed that rituximab produced a similar cohort-level serologic trend but through distinct cellular mechanisms and with different inter-individual response patterns.

A key limitation is that the CLE/SLE UISS extension has not yet been quantitatively calibrated to longitudinal patient-level clinical or molecular measurements (e.g. CLASI scores, interferon signatures, serial anti-Ro/SSA, and anti-La/SSB titers). Accordingly, the present results should be interpreted as mechanistic hypotheses and cohort-level trend analyses rather than calibrated clinical forecasts. While the model reproduces qualitative and semi-quantitative biological behaviors consistent with published observations, formal parameter inference against longitudinal datasets has not yet been performed. Future work will focus on systematic calibration using Bayesian and likelihood-free inference frameworks applied to longitudinal serologic, cellular, and clinical severity measurements, enabling posterior predictive validation and uncertainty quantification. The CLE-ABM comprises multiple interacting parameters governing cellular activation thresholds, cytokine response curves, survival kinetics, and antigen dynamics. Although stochastic cohort generation and bootstrap analyses provide insight into outcome variability, formal assessment of parameter identifiability, global sensitivity, and uncertainty propagation was not undertaken in this study. Consequently, robustness claims should be interpreted in terms of mechanistic consistency and cohort-level trend stability rather than parameter-level determinability. An additional direction for external validation is comparison against non-CLE reference datasets, including healthy skin and other inflammatory dermatoses such as psoriasis. Such analyses would help assess the extent to which the emergent cellular and antigen presentation programs reproduced by the model are CLE-specific rather than shared inflammatory features. This lies beyond the scope of the present mechanistic study but represents an important next step in model evaluation.

In summary, our agent-based simulations provide a mechanistic explanation for why belimumab yields modest median reductions in Ro/La IgG across a heterogeneous cohort, while producing larger decreases in a subset of patients. In contrast, rituximab robustly depletes $CD20^{+}$ B-cell compartments (naïve, activated, memory), leading to frequent and sometimes deep reductions in plasmablast-driven output. Overall, the model emphasizes that the balance between plasmablasts and LLPCs is a primary determinant of serologic response, motivating biomarker-guided strategies and combination therapies to improve response rates. We release the model and analysis scripts to support independent testing and calibration in longitudinal cohorts. Beyond SLE/CLE, the framework is modular and generalizable: UISS separates physiology, disease, and therapy layers, with disease-specific behavior encoded in a replaceable disease layer defining tissue microenvironment, antigen repertoire, and local immune interactions. Therapeutic effects are implemented as modular interventions (PK/PD, mechanisms, and cell-level rules), enabling in silico evaluation of alternative drugs, schedules, and combinations. In addition, the therapeutic modules have not yet been quantitatively calibrated against clinical trial datasets for belimumab or rituximab. Therefore, reported treatment effects should be interpreted as mechanistic response patterns rather than validated effect-size predictions. Future work will incorporate longitudinal clinical trial data, including serologic endpoints, B-cell depletion kinetics, and disease activity scores, to enable quantitative model calibration and translational validation.

Methods

The CLE-focused ABM was developed as an extension of the UISS, a validated agent-based immune modeling framework that provides baseline immune system dynamics [11, 45], including hematopoiesis, antigen encoding and presentation, MHC-restricted T-cell activation, stochastic rule execution, stochastic cell–cell interaction rules, cytokine diffusion fields, compartmental organization, and a generic pharmacokinetic/pharmacodynamic (PK/PD) interface for therapeutic simulation. While UISS supplies this general immune simulation infrastructure, we implemented a CLE-specific disease layer on top of the core engine. In contrast to previous UISS applications, we introduced a skin lesion compartment (epidermis/dermis lattice), modules capturing UV-induced keratinocyte apoptosis, explicit Ro/SSA and La/SSB autoantigen release, type I interferon amplification loops, Teff/Treg imbalance thresholds, and CLE-specific B-cell isotype switching dynamics. The therapeutic layer was further extended to incorporate belimumab (BAFF neutralization) and rituximab (anti-CD20 depletion), enabling simulation of B-cell targeted interventions. These disease-specific extensions operate within the baseline UISS immune environment and allow generation of digital patients to explore flare heterogeneity and treatment response variability in CLE.

Model architecture

Our ABM architecture integrates three layers: (i) a physiological layer capturing baseline immune function, (ii) a disease layer

Downloaded from academic.oup.com/bib/article/27/4/bbag416/8750276 by Universita' degli Studi di Catania user on 30 September 2026

simulating lupus-related dysregulation in the skin and systemic compartments, and (iii) a treatment layer allowing pharmacological interventions. Overview of CLE-based ABM model (Fig. 1A), distinguishing between the skin lesion compartment (epidermis and dermis) and the lymph node/blood compartment. Key processes include UV-induced keratinocyte apoptosis and autoantigen release, antigen presentation by dendritic cells, Teff/Treg balance, and B-cell driven autoantibody generation.

For transparency and mechanistic detail, the complete conceptual and mechanistic interaction map is provided in Fig. 6.

The structural interaction topology shown in Fig. 6 reflects established CLE/SLE immunopathology, including UV-induced keratinocyte apoptosis and autoantigen exposure [21, 26, 44], type I interferon amplification mediated by plasmacytoid dendritic cells [24, 26, 34], dendritic cell antigen presentation and T-cell polarization [3, 23, 32], BAFF-dependent B-cell survival and plasmablast differentiation [19, 37, 42], and immune complex-driven complement activation and tissue injury [22, 28, 39]. These structural links were defined a prior from literature and encoded as rule-based transitions and parameter tuning modulates interaction strength but does not introduce new topological connections.

Role of universal immune system simulator framework and CLE-specific extensions

Physiological layer

The physiological layer describes how the immune system distinguishes self from nonself under healthy conditions, encompassing processes such as hematopoiesis, thymic selection, B-cell repertoire diversification, and antibody hypermutation. This layer provides the baseline immune dynamics upon which disease-specific perturbations are superimposed.

Disease layer: cutaneous lupus erythematosus implementation

The disease layer captures CLE-specific mechanisms, with a focus on UV-driven skin inflammation and autoantibody-mediated injury.

Keratinocyte damage and antigen release

The skin-focused disease module implements key CLE mechanisms, emphasizing UV-driven keratinocyte injury, Ro/SSA and La/SSB autoantigen release, antigen presentation, and autoantibody dynamics. It is lattice-based and includes discrete agents for keratinocytes, antigens, antigen-presenting cells (APCs), T cells, B cells, and plasma cells. The main rules and mathematical expressions are summarized in the (Supplementary Methods (Keratinocyte principal rules and mathematical expressions)).

Antigen composition and presentation

Antigen compositions are represented as block structures storing peptide indices, epitopes, and PAMP flags. Upon injection or release from dying keratinocytes, antigen entries are reused or created via `create_Ag_entry()`), then attached to the lattice site through `ANTIGEN` records in `AGLIST[x]`. Type I interferon signaling is modeled by IFN-α/IFN-β production from damaged keratinocytes and APCs, which modulates downstream activation probabilities for B and T cells.

T-cell compartments and Teff/Treg balance

Effector and regulatory T cells are modeled as discrete agents with rules for activation, cytokine production, and suppression. Effector subsets (aggregating Th1/Th17-like behavior) increase inflammation by enhancing APC activation and IFN-γ/IL-21 production, whereas Tregs suppress APC activation and reduce local B cell activation probability. Dysregulation occurs when pro-inflammatory cytokines exceed suppressive capacity, causing probabilistic control failure, and potentially sustained flares.

B-cell activation, isotype switching, and plasma cells

B-cells activate upon recognizing cognate antigen presented by APCs. Once activated, they proliferate, undergo hypermutation, and differentiate into plasmablasts or plasma cells. Isotype switching depends on the local cytokine milieu, with switch probabilities defined as functions of cytokine concentrations (e.g. IL-21 and IFN-γ promote IgG; IL-4 promotes IgE/IgG; TGF-β promotes IgA). Plasma cells secrete antibodies each timestep, and LLPCs are implicitly represented as a long half-life PLB subpopulation (`tau`), making them relatively insensitive to BAFF neutralization.

Cytokine network and coupling

Cytokine fields are represented as spatially local scalar variables that are updated at each timestep by release functions. Event propensities are functions of local cytokine concentrations, implemented either as sigmoid or exponential response curves and sampled stochastically. For example, B-cell duplication and isotype switching are governed by functions

$$p_{\text{dup}} = f_{\text{dup}}(\text{BAFF},\ \text{IL-21}), \qquad p_{\text{switch}} = f_{\text{switch}}(\text{IFN-}\gamma,\ \text{IL-4},\ \text{TGF-}\beta),$$

which are mapped in code to numerical probabilities used by the Bernoulli sampler.

Treatment layer: cutaneous lupus erythematosus therapy implementation

As the CLE treatment layer, we implemented two clinically relevant B-cell–targeted interventions belimumab (BAFF neutralization) and rituximab (anti-CD20 depletion). For each experimental condition, we ran paired stochastic simulations: a control (pretherapy) and a treatment (post-therapy) replicate for each random seed, with identical model parameters between members of a pair except for the specified therapeutic dosing applied in the post-therapy run. We performed $N = 50$ independent replicate pairs (distinct RNG seeds).

Belimumab implementation

Belimumab is modeled as a noncellular field $\mathbf{Belmu}_x(t)$ that stores the drug mass (micrograms) at lattice patch x. Injections are simulated by the function `release_Belmu(x, qty)` which increments $\mathbf{Belmu}_x$ by the administered mass. Complete details about the Belimumab therapy, including implementation, dosing, pharmacodynamics, Autoantigen registration (Ro/SSA, La/SSB, Outcome variables & file format, Time alignment & baseline definition, Percent-change metrics, Aggregation across stochastic replicates, and Bootstrap confidence intervals for medians, are explained in the (Supplementary Methods. Belimumab implementation and pharmacodynamics).

Downloaded from academic.oup.com/bib/article/27/4/bbag416/8750276 by Universita' degli Studi di Catania user on 30 September 2026

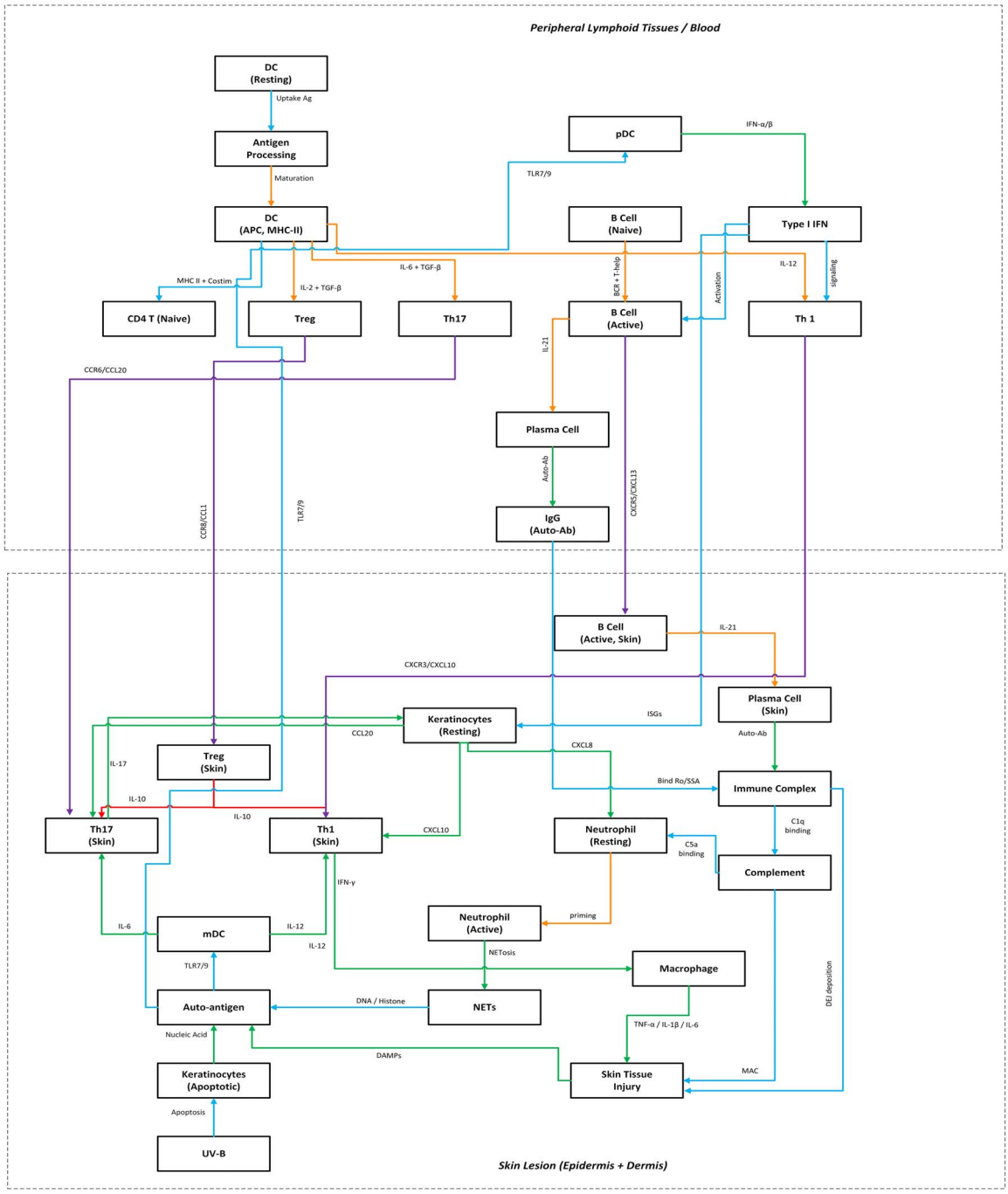


Figure 6 Mechanistic architecture of the CLE disease layer implemented in UISS. The model distinguishes two interacting compartments: (i) peripheral lymphoid tissues/blood (top) and (ii) the skin lesion microenvironment (epidermis and dermis; bottom). Rectangles represent modeled cell populations or molecular pools, and directed arrows denote literature supported causal interactions encoded as rule-based transitions in the ABM. UV-B exposure induces keratinocyte apoptosis, leading to release of nuclear autoantigens including Ro/SSA and La/SSB. These antigens are captured by dendritic cells (DCs), which undergo maturation and present antigen via MHC-II to naïve $CD4^+$ T cells. Type I interferon (IFN-α/β), produced by plasmacytoid DCs and damaged keratinocytes, amplifies antigen presentation and promotes effector differentiation. Effector T cells (Th1/Th17 like) secrete IFN-γ, IL-21, and IL-17, enhancing B-cell activation and inflammatory recruitment, while regulatory T cells (Tregs) suppress APC activation and effector expansion. B cells recognizing cognate autoantigen undergo activation, proliferation, and differentiation into plasmablasts and plasma cells. Class-switch recombination is influenced by the cytokine milieu (e.g. IL-21, IFN-γ). Plasma cells secrete IgG autoantibodies, which bind released autoantigens to form immune complexes. These complexes activate complement pathways, promote neutrophil priming and NET formation, and contribute to sustained tissue injury. LLPCs persist independently of BAFF signaling and sustain antibody production. All depicted interactions are grounded in established CLE/SLE immunopathology literature and implemented as explicit rule-based transitions in the CLE-ABM. Color coding indicates process categories: differentiation/activation (orange), secretion (green), interaction/binding (blue), chemokine-mediated trafficking (purple), and regulatory suppression (red).

Downloaded from academic.oup.com/bib/article/27/4/bbag416/8750276 by Universita' degli Studi di Catania user on 30 September 2026

Rituximab implementation

Rituximab is modeled as an anti-CD20 biologic that depletes $CD20^{+}$ B cells (naïve, activated, and memory subsets) while sparing CD20-negative plasma cells (PLBs/LLPCs). Rituximab is implemented as a spatially distributed drug field $\mathbf{Ritux}_x(t)$ (micrograms) defined per lattice patch x; injections call the simulator function `release_Ritux(x,qty)` which increments the local mass.

Complete details about the Rituximab therapy, including implementation, clearance, per-cell depletion probability, scheduling & dose, selective and biological assumptions, outcome variables, and parameterization & sensitivity, are explained in the (Supplementary Methods. Rituximab implementation and pharmacodynamics).

Agent-based model digital patient generation

To capture inter-individual heterogeneity, we generated digital patients by varying initial immune parameters (e.g. Treg fitness, BAFF levels, UV sensitivity, cytokine responsiveness) using stochastic sampling. This approach enabled simulation of various flare frequencies, antibody dynamics, and therapy responses across a virtual CLE cohort, reflecting the heterogeneity observed in clinical populations.

We generated cohorts of 50 digital patients, following the complete approach described [46]. In real clinical settings, each patient is defined by a combination of biological and pathophysiological parameters that together establish an individual immunological profile. To replicate this heterogeneity *in silico* while preserving biological plausibility for feeding into the UISS simulator, each parameter in the feature vector was assigned a single value and systematic variation of these values was produced in multiple feature vectors representing distinct virtual patients. To ensure biological plausibility, parameter ranges were defined within physiologically meaningful intervals informed by published lupus immunology literature and baseline immune homeostasis constraints implemented in UISS. Parameters governing Treg fitness, BAFF concentration, UV sensitivity, cytokine responsiveness, and B-cell survival were bounded to avoid nonphysiological immune collapse activation states.

Sampling was performed using truncated continuous distributions to prevent extreme outliers while preserving heterogeneity. In addition, correlations between biologically coupled parameters were explicitly imposed when generating feature vectors. For example, BAFF levels were positively coupled with B-cell survival probabilities, and reduced Treg fitness was correlated with increased effector activation propensity. These correlations were implemented using a structured covariance matrix applied to the 22-dimensional feature vector prior to simulation, ensuring that virtual patients represent coherent immunological profiles rather than independently perturbed parameters. This approach follows previously described UISS digital patient generation methodology [46], which aims to reproduce inter-individual variability while maintaining internal biological consistency.

In particular, the feature vector consists of 22 input variables, yielding 231 possible pairwise correlations ($22 \times 21/2$). For a standard mathematical biological formulation, see the Supplementary Methods. Mathematical implementation of feature vectors. For simulation environment details (Supplementary Methods. Simulation environment). While stochastic perturbation of biologically constrained parameters enables exploration of inter-individual heterogeneity, formal structural identifiability analysis, and global sensitivity quantification were not performed in this study. The present work focuses on mechanistic behavior and cohort-level variability rather than parameter inference.

Single-cell RNA sequence reference data and preprocessing (GSE179633)

We obtained scRNA-seq data from the GEO accession GSE179633 [15] and preprocessed to restrict the analyses to DLE samples, keeping the epidermis, and dermis as separate compartments. The scRNA-seq reference is used not only for descriptive comparison, but also to inform the definition of model compartments and cell states (epidermis versus dermis, T and myeloid subtypes, UV-stress signatures in keratinocytes), thereby constraining the design of CLE-ABM and providing a single-cell anchored reference for subsequent structural validation. The cells and genes were prefiltered and kept cells within 200–7000 detected genes using standard quality criteria (library size and mitochondrial content $< 12\%$), normalized (total-count scaling and log transform where target sum set as "1e4"), and for making the analysis memory friendly, we union the per-sample highly variable genes (HVGs) by setting Seurat_v3, 5000 n_top_genes and selected HVGs that are highly variable in any batch (sample), and reduced by PCA; neighbors and UMAP were computed. All major classes for each tissue epidermis and dermis were clustered by Leiden, which includes keratinocytes, T, Macro/DC, Melanocytes, NK, B, and Fibroblast, T, Endothelial, Macro/DC, Mast, NK, Schwann, respectively. The present benchmarking focused on cross-sectional cellular composition and mechanistic consistency with lesion-level transcriptomic data. The model was not quantitatively calibrated to longitudinal clinical trajectories in this study.

Complete details of the computational environment and single-cell analysis toolkits, including their implementation in the code, are provided in the (Supplementary Methods. Computational environment and single-cell toolkits).

Key Points

- A new integrative cutaneous lupus erythematosus agent-based model (CLE-ABM) is introduced, extending the universal immune system simulator framework to mechanistically capture ultraviolet-driven keratinocyte injury, type I interferon loops, T-cell imbalance, B-cell activation, and autoantibody production in cutaneous lupus.
- Single-cell RNA-seq benchmarking (GSE179633) demonstrates that digital patients reproduce key cellular compositions and epithelial programs seen in discoid lupus erythematosus lesions, while highlighting actionable gaps (e.g. Th17/Treg imbalance, myeloid subset calibration).
- Digital patient ensembles capture inter-individual heterogeneity, reproducing diverse flare trajectories, IgG kinetics, and immune-cell dynamics that reflect the clinical variability of CLE/SLE.
- *In silico* therapy simulations of belimumab and rituximab show modest cohort-level reductions in Ro/La IgG but substantial heterogeneity, with strong responses confined to subsets driven by BAFF-sensitive plasmablasts rather than long-lived plasma cell-dominated profiles.
- The modeling platform is modular and generalizable, allowing rapid adaptation to other autoimmune diseases and serving as a foundation for future calibration, biomarker-guided stratification, and virtual clinical trial design.

Downloaded from academic.oup.com/bib/article/27/4/bbag416/8750276 by Universita' degli Studi di Catania user on 30 September 2026

Acknowledgements

The authors acknowledge the support and training provided by the European Union's MSCA Doctoral Network "SIGNATURE."

Author contributions

Abdul Wahab (Conceptualization, Analysis, Visualization, and Methodology, Writing Original Draft Preparation, Writing, Review, and Editing, Final Review, and Editing), Giulia Russo (Conceptualization, Writing, Review, and Editing, Final Review and Editing), Francesco Pappalardo (Conceptualization, Writing, Review, and Editing, Final Review and Editing). All authors read and approved the final manuscript.

Supplementary material

Supplementary material is available at *Briefings in Bioinformatics* online.

Conflicts of interest

None declared.

Funding

This project has received funding from the European Union's Horizon Europe research and innovation programme under grant agreement No. 101072891.

Data availability

Single-cell data used in this study come from publicly available sources GSE179633 [15]. The data of digital patients generated in this work are available on GitHub at https://github.com/abdul-bioinfo/CLE-ABM.git

Raw simulation data are available on GitHub at https://github.com/abdul-bioinfo/CLE-ABM.git

Ethics and Consent to Participate declarations

Not applicable.

References

1. Wenzel J. Cutaneous lupus erythematosus: new insights into pathogenesis and therapeutic strategies. *Nat Rev Rheumatol* 2019; **15**:519–32.
2. Patel J, Borucki R, Werth VP. An update on the pathogenesis of cutaneous lupus erythematosus and its role in clinical practice. *Curr Rheumatol Rep* 2020; **22**:69.
3. Fetter T, Braegelmann C, deVos L *et al.* Current concepts on pathogenic mechanisms and histopathology in cutaneous lupus erythematosus. *Front Med* 2022; **9**:915828.
4. Sestak AL, Fürnrohr BG, Harley JB *et al.* The genetics of systemic lupus erythematosus and implications for targeted therapy. *Ann Rheum Dis* 2011; **70**:i37–43.
5. Fetter T, Wenzel J. Cutaneous lupus erythematosus: the impact of self-amplifying innate and adaptive immune responses and future prospects of targeted therapies. *Exp Dermatol* 2020; **29**:1123–32.
6. Lashgari D, Merino Tejero E, Meyer-Hermann M *et al.* From affinity selection to kinetic selection in germinal Centre modelling. *PLoS Comput Biol* 2022; **18**:e1010168.
7. Merino Tejero E, Lashgari D, García-Valiente R *et al.* Multiscale modeling of germinal center recapitulates the temporal transition from memory B cells to plasma cells differentiation as regulated by antigen affinity-based Tfh cell help. *Front Immunol* 2021; **11**:620716.
8. Yazdani A, Bahrami F, Pourgholaminejad A *et al.* A biological and a mathematical model of SLE treated by mesenchymal stem cells covering all the stages of the disease. *Theory Biosci* 2023; **142**:167–79.
9. Wendelsdorf K, Bassaganya-Riera J, Hontecillas R *et al.* Model of colonic inflammation: immune modulatory mechanisms in inflammatory bowel disease. *J Theor Biol* 2010; **264**:1225–39.
10. Goteti K, Garcia R, Gillespie WR *et al.* Model-based meta-analysis using latent variable modeling to set benchmarks for new treatments of systemic lupus erythematosus. CPT: pharmacometrics & Systems. *Pharmacology* 2024; **13**:281–95.
11. Pappalardo F, Pennisi M, Motta S. Universal immune system simulator framework (UISS). In: *Proceedings of the First ACM International Conference on Bioinformatics and Computational Biology*, NY, USA: Niagara Falls, pp. 649–50, 2010.
12. An G, Fitzpatrick B, Christley S *et al.* Optimization and control of agent-based models in biology: a perspective. *Bull Math Biol* 2017; **79**:63–87.
13. Wahab A, Russo G, Pappalardo F. Agent-based modeling of cutaneous lupus erythematosus: exploring keratinocyte-driven mechanisms. In: *2024 IEEE International Conference on Bioinformatics and Biomedicine (BIBM)*, Lisboa, Portugal, pp. 6667–71. IEEE, 2024.
14. Pennisi M, Russo G, Sgroi G *et al.* Predicting the artificial immunity induced by RUTI® vaccine against tuberculosis using universal immune system simulator (UISS). *BMC Bioinformatics* 2019; **20**:504.
15. Zheng M, Hu Z, Mei X *et al.* Single-cell sequencing shows cellular heterogeneity of cutaneous lesions in lupus erythematosus. *Nat Commun* 2022; **13**:7489.
16. Werth VP. Clinical manifestations of cutaneous lupus erythematosus. *Autoimmun Rev* 2005; **4**:296–302.
17. Bonelli M, Savitskaya A, Von Dalwigk K *et al.* Quantitative and qualitative deficiencies of regulatory T cells in patients with systemic lupus erythematosus (SLE). *Int Immunol* 2008; **20**:861–8.
18. Albrecht J, Taylor L, Berlin JA *et al.* The CLASI (cutaneous lupus erythematosus disease area and severity index): an outcome instrument for cutaneous lupus erythematosus. *J Invest Dermatol* 2005; **125**:889–94.
19. Grammer AC, Lipsky PE. B cell abnormalities in systemic lupus erythematosus. *Arthritis Res Ther* 2003; **5**:S22.
20. Tuffanelli DL. Lupus erythematosus. *Arch Dermatol* 1972; **106**:553–66.
21. Werth VP, Bashir M, Zhang W. Photosensitivity in rheumatic diseases. In: *Journal of Investigative Dermatology Symposium Proceedings*, Vol. **9**, pp. 57–63. Elsevier, 2004.
22. Wahren-Herlenius M, Dörner T. Immunopathogenic mechanisms of systemic autoimmune disease. *Lancet* 2013; **382**:819–31.
23. Banchereau J, Steinman RM. Dendritic cells and the control of immunity. *Nature* 1998; **392**:245–52.
24. Blanco P, Palucka AK, Gill M *et al.* Induction of dendritic cell differentiation by IFN-α in systemic lupus erythematosus. *Science* 2001; **294**:1540–3.
25. Leonard D, Eloranta ML, Hagberg N *et al.* Activated T cells enhance interferon-α production by plasmacytoid dendritic cells stimulated with RNA-containing immune complexes. *Ann Rheum Dis* 2016; **75**:1728–34.

Downloaded from academic.oup.com/bib/article/27/4/bbag416/8750276 by Universita' degli Studi di Catania user on 30 September 2026

26. Sarkar MK, Hile GA, Tsoi LC *et al.* Photosensitivity and type I IFN responses in cutaneous lupus are driven by epidermal-derived interferon kappa. *Ann Rheum Dis* 2018; **77**:1653–64.
27. Folzenlogen D, Hofer M, Leung D *et al.* Analysis of CD80 and CD86 expression on peripheral blood B lymphocytes reveals increased expression of CD86 in lupus patients. *Clin Immunol Immunopathol* 1997; **83**:199–204.
28. Maz MP, Martens JW, Hannoudi A *et al.* Recent advances in cutaneous lupus. *J Autoimmun* 2022; **132**:102865.
29. Vermi W, Lonardi S, Morassi M *et al.* Cutaneous distribution of plasmacytoid dendritic cells in lupus erythematosus. Selective tropism at the site of epithelial apoptotic damage. *Immunobiology* 2009; **214**:877–86.
30. Dunlap GS, Billi AC, Xing X *et al.* Single-cell transcriptomics reveals distinct effector profiles of infiltrating T cells in lupus skin and kidney. *JCI Insight* 2022; **7**:e156341.
31. Ryan GE, Harris JE, Richmond JM. Resident memory T cells in autoimmune skin diseases. *Front Immunol* 2021; **12**:652191.
32. Jabbari A, Suárez-Fariñas M, Fuentes-Duculan J *et al.* Dominant Th1 and minimal Th17 skewing in discoid lupus revealed by transcriptomic comparison with psoriasis. *J Invest Dermatol* 2014; **134**:87–95.
33. Gutiérrez-Martínez E, Planès R, Anselmi G *et al.* Cross-presentation of cell-associated antigens by MHC class I in dendritic cell subsets. *Front Immunol* 2015; **6**:363.
34. Karnell JL, Wu Y, Mittereder N *et al.* Depleting plasmacytoid dendritic cells reduces local type I interferon responses and disease activity in patients with cutaneous lupus. *Sci Transl Med* 2021; **13**:eabf8442.
35. Auböck J, Romani N, Grubauer G *et al.* HLA-DR expression on keratinocytes is a common feature of diseased skin. *Br J Dermatol* 1986; **114**:465–72.
36. Skopelja-Gardner S, An J, Tai J *et al.* The early local and systemic type I interferon responses to ultraviolet B light exposure are cGAS dependent. *Sci Rep* 2020; **10**:7908.
37. Stohl W, Hiepe F, Latinis KM *et al.* Belimumab reduces autoantibodies, normalizes low complement levels, and reduces select B cell populations in patients with systemic lupus erythematosus. *Arthritis Rheum* 2012; **64**:2328–37.
38. Chen W, Hong SH, Jenks SA *et al.* Distinct transcriptomes and autocrine cytokines underpin maturation and survival of antibody-secreting cells in systemic lupus erythematosus. *Nat Commun* 2024; **15**:1899.
39. Hassan AB, Lundberg IE, Isenberg D *et al.* Serial analysis of Ro/SSA and La/SSB antibody levels and correlation with clinical disease activity in patients with systemic lupus erythematosus. *Scand J Rheumatol* 2002; **31**:133–9.
40. Parodis I, Åkerström E, Sjöwall C *et al.* Autoantibody and cytokine profiles during treatment with belimumab in patients with systemic lupus erythematosus. *Int J Mol Sci* 2020; **21**: 3463.
41. Vital EM, Dass S, Buch MH *et al.* B cell biomarkers of rituximab responses in systemic lupus erythematosus. *Arthritis Rheum* 2011; **63**:3038–47.
42. Shin W, Lee HT, Lim H *et al.* BAFF-neutralizing interaction of belimumab related to its therapeutic efficacy for treating systemic lupus erythematosus. *Nat Commun* 2018; **9**:1200.
43. Lightman SM, Utley A, Lee KP. Survival of long-lived plasma cells (LLPC): piecing together the puzzle. *Front Immunol* 2019; **10**:965.
44. Estadt SN, Maz MP, Musai J *et al.* Mechanisms of photosensitivity in autoimmunity. *J Invest Dermatol* 2022; **142**:849–56.
45. Pappalardo F, Pennisi M, Chiacchio F *et al.* GRIDUISS–A grid based universal immune system simulator framework. In:*International Conference on Intelligent Computing*, pp. 285–90. Springer, 2010.
46. Juárez MA, Pennisi M, Russo G *et al.* Generation of digital patients for the simulation of tuberculosis with UISS-TB. *BMC Bioinformatics* 2020; **21**:449.

Downloaded from academic.oup.com/bib/article/27/4/bbag416/8750276 by Universita' degli Studi di Catania user on 30 September 2026

© The Author(s) 2026. Published by Oxford University Press. This is an Open Access article distributed under the terms of the Creative Commons Attribution-NonCommercial License (https://creativecommons.org/licenses/by-nc/4.0/), which permits non-commercial re-use, distribution, and reproduction in any medium, provided the original work is properly cited. For commercial re-use, please contact reprints@oup.com for reprints and translation rights for reprints. All other permissions can be obtained through our RightsLink service via the Permissions link on the article page on our site—for further information please contact journals.permissions@oup.com.
Briefings in Bioinformatics, 2026, **27**, bbag416
https://doi.org/10.1093/bib/bbag416
Problem Solving Protocol